J. Fluid Mech. (1992), *vol.* 245, *pp.* 413–435

Field observations of orbital velocities and pressure in weakly nonlinear surface gravity waves

By T. H. C. HERBERS, R. L. LOWE AND R. T. GUZA

Center for Coastal Studies, 0209, Scripps Institution of Oceanography, La Jolla, CA 92093, USA

(Received 28 January 1992 and in revised form 16 June 1992)

Field measurements of wave orbital velocities and pressure, collected in the lower part of the water column in 7 m depth with a three-component acoustic Doppler current meter and a co-located pressure transducer, are compared to the second-order theory for weakly nonlinear surface gravity waves in arbitrary water depth (Hasselmann 1962). Pressure and velocity spectra and cross-spectra are in excellent agreement with (linear) free wave transfer functions, even at (and higher than) twice the spectral peak frequency where nonlinearities (forced secondary waves) are expected to be important. Theoretical predictions show that although secondary waves sometimes contribute a significant fraction of the energy observed at double swell and sea frequencies, their effect on velocity–pressure transfer functions is small. However, forced waves are more apparent in deviations from Gaussian statistics. Good agreement between observed and predicted third-order statistics shows that Hasselmann's weakly nonlinear theory accurately describes the secondary pressure and orbital velocity (both horizontal and vertical components) field at double swell and sea frequencies, even for moderately large ($O(0.1$–$0.2)$) values of the nonlinear perturbation parameter. Only with near-breaking swell and relatively strong nonlinearities (perturbation parameter ≈ 0.22), do the observed third-order statistics diverge significantly from Hasselmann's theory.

1. Introduction

Theories for weakly nonlinear surface gravity waves based on a perturbation expansion have been developed by various authors (Phillips 1960; Hasselmann 1962; and others). The lowest order (primary) wave components are free waves obeying the linear dispersion relation. At the next order secondary wave components are generated in nonlinear triad interactions with two primary wave components. Triad interactions are not resonant when the primary waves are in deep and intermediate depths; resonances first occur in quartet interactions between three primary waves and a tertiary wave (e.g. Phillips, 1960). Hence, in intermediate and deep water secondary waves are forced waves, not obeying the dispersion relation. Phase-coupling of primary and secondary waves causes non-Gaussian statistics (e.g. Hasselmann, Munk & MacDonald 1963; Longuet-Higgins 1963), for example distorting a lowest-order Gaussian sea surface of statistically independent primary wave components to a profile with steeper crests and flatter troughs.

In deep water ($kh \gg 1$, with k the wavenumber of the primary waves and h the water depth) typical secondary wave contributions are very weak and often not detectable in sea surface elevation measurements (e.g. Komen 1980; Donelan, Hamilton & Hui 1985; Laing 1986). However, relatively long-wavelength secondary

waves, forced by directionally opposing primary waves, are an important source of small-amplitude pressure fluctuations observed at depths large compared to the wavelengths of sea and swell where free wave pressure is strongly attenuated (e.g. Webb & Cox 1986; Cox & Jacobs 1989). Energy levels and wavenumbers of secondary pressure fluctuations observed at the sea floor in relatively deep water ($kh \approx 3$), are consistent with the predictions of Hasselmann's (1962) weakly nonlinear theory (Herbers & Guza 1991, 1992).

The very strong near-resonant amplification of harmonics and associated asymmetric wave forms (i.e. steep forward faces) of nonlinear shoaling waves prior to breaking are not well modelled by Hasselmann's (1962) theory but are accurately predicted by the Boussinesq equations (e.g. Peregrine 1967; Grimshaw 1970; Freilich & Guza 1984; Liu, Yoon & Kirby 1985; Elgar & Guza 1985). The pronounced deviations from linear Gaussian statistics of surface waves in very shallow water ($kh \ll 1$) are readily detected (e.g. Guza & Thornton 1985; Elgar, Freilich & Guza 1990).

The present study concerns the local nonlinearity of naturally occurring surface gravity waves in moderately shallow to intermediate depth water ($kh = 0.3$–0.9), well seawards of the zone of sustained wave breaking. A three-component acoustic Doppler current meter (Herbers, Lowe & Guza 1991) and a pressure transducer were mounted on the sea bed in 7 m depth, where local nonlinear effects are enhanced relative to deep water but still small enough that Hasselmann's (1962) weakly nonlinear theory is potentially valid. Hasselmann *et al.* (1963) show that third-order statistics of wave pressure observations are qualitatively consistent with weakly nonlinear theory in a similar environment. However, field verifications of nonlinear effects on the wave orbital velocity field are presently lacking, possibly because existing *in-situ* current meters have not been accurate enough to measure relatively weak secondary flows. It is shown in the present study that the nonlinearity of wave-induced pressures and orbital velocities are accurately predicted by Hasselmann's theory for a wide range of wave conditions. The field experiment and gross properties of the observed wave fields are described in §2. In §3, the nonlinear theory is briefly reviewed and the (weak) dependence of secondary wave energy on the (refractively columnated) directional spectrum of primary waves is discussed. In §4, pressure and velocity spectra and cross-spectra are compared to the theoretical transfer functions for both free (primary) and forced (secondary) waves. Non-Gaussian statistics associated with phase-coupled wave triads are estimated and compared to theoretical predictions in §5. The results are summarized in §6.

2. Description of observations

An acoustic Doppler current meter and a pressure transducer were deployed in 7 m depth on a fine-grained, gently sloping (1°) sea bed near Scripps Institution of Oceanography in La Jolla, California. The acoustic Doppler instrument (figure 1; Herbers *et al.* 1991) contains four pairs (i.e. transmitter and receiver) of 1 MHz acoustic transducers. Each of the four beams looks upward, 45° ($\pm 1°$) inclined from vertical, and measures the alongbeam velocity at a range of 1 m. The four sample volumes are at the corners of a square in the horizontal plane at an elevation of 2.5 m above the bed. The instrument has the important advantage over *in-situ* current meters, used in previous field studies of wave orbital velocities (e.g. Bowden & White 1966; Simpson 1969; Thornton & Krapohl 1974; Guza & Thornton 1980; Battjes & van Heteren 1984; Guza *et al.* 1988; and others) that the sample volume is not in

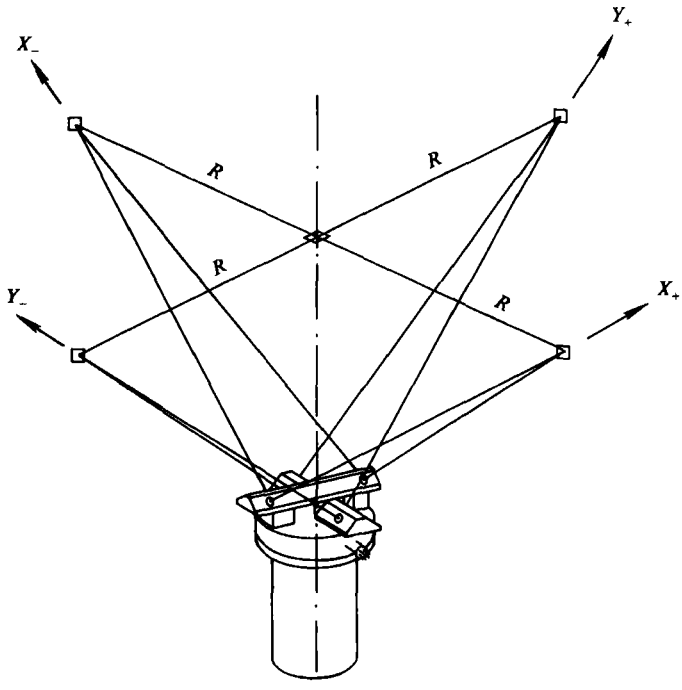

FIGURE 1. Geometry of the acoustic Doppler current meter. Four beam pairs (X_+, X_-, Y_+ and Y_-) each measure the alongbeam velocity component at a single range of 1 m. The four sample volumes form a square with dimension $R\sqrt{2} = 1$ m in the horizontal plane at an elevation of 2.5 m above the sea bed (from Herbers *et al.* 1991).

close proximity to the instrument and therefore the measured flow field is not disturbed by an intrusive probe. The pressure transducer was buried a few cm within the sea bed (to minimize flow noise), directly underneath the current meter. Limited field comparisons of orbital velocity and pressure measurements under small-amplitude surface waves, using an earlier version of the present acoustic Doppler velocimeter, show close agreement with the theoretical transfer functions for linear waves over a wide frequency range (errors typically less than 5% in the range 0.08–0.30 Hz) (Herbers *et al.* 1991).

The data processing scheme applied to the acoustic Doppler data is described in Appendix A. The four acoustic beam measurements can be linearly combined to estimate the three orthogonal wave orbital velocity components u (cross-shore), v (alongshore), and w (vertical). Owing to the finite separation of the sample volumes (figure 1), the estimated velocity components ($\hat{u}$, $\hat{v}$, $\hat{w}$) differ from (u, v, w) by $O(kR)$ where $R = 0.71$ m and k is the wavenumber (Appendix A, equation (A3)). This $O(kR)$ bias is taken into account and the remaining $O(kR)^2$ bias errors are negligibly small in the frequency range considered here (Appendix A).

Velocity and pressure data were collected for between 1 and 2 hours on ten occasions in Spring 1991. The root-mean-square fluctuations of bottom pressure $p_{\rm rms}$ and surface elevation $\eta_{\rm rms}$ (obtained from the measured bottom pressure spectrum with a linear theory depth correction) over the frequency range 0.05–0.25 Hz, and other bulk wave statistics discussed below, are listed in table 1. The observations include both energetic waves (significant wave height $\equiv 4\eta_{\rm rms} > 1$ m) for which the theoretically predicted nonlinear effects are significant, and calms (significant wave heights < 0.5 m) when relatively weak nonlinearity is expected.

Date (1991)	p_{rms} (cm)	η_{rms} (cm)	$\bar{f}$ (Hz)	σ_f (Hz)	$\bar{\theta}$ (deg.)	σ_θ (deg.)	G_{tot}	α
29 March	9.3	13.2	0.14	0.04	4.9	17.3	1.016	0.051 (0.057)
30 March	9.9	13.0	0.12	0.04	0.4	16.4	1.017	0.071 (0.078)
03 April	19.7	25.6	0.12	0.03	−0.2	12.4	0.997	0.109 (0.124)
08 April	24.6	30.4	0.11	0.04	−3.4	12.2	1.002	0.216 (0.236)
10 April	20.2	26.2	0.12	0.03	−0.8	13.7	1.001	0.093 (0.107)
29 April	16.7	21.4	0.12	0.04	−2.4	13.5	0.997	0.128 (0.140)
30 April	16.0	19.5	0.10	0.04	−3.1	13.6	1.006	0.184 (0.196)
01 May	17.1	22.5	0.12	0.04	0.4	15.6	1.001	0.120 (0.132)
10 May	25.6	32.7	0.12	0.03	−2.5	13.5	1.007	0.159 (0.178)
22 May	8.6	11.2	0.12	0.05	4.3	19.0	1.011	0.076 (0.082)

TABLE 1. Summary of wave statistics. Listed are root-mean-square pressure (p_{rms}) and surface elevation (η_{rms}) fluctuations, the mean frequency ($\bar{f}$) and propagation direction ($\bar{\theta}$) and the corresponding standard deviations (σ_f and σ_θ), the normalized velocity–pressure ratio G_{tot}, equation (12), and the ratio α, equation (15), between $p_{rms,forced}$ (root-mean-square value of secondary pressure fluctuations, equation (14a)) and p_{rms}. The values enclosed in parentheses are estimates of α that neglect the (small) contribution of the local flow field (2a) to $p_{rms,forced}$.

Estimates of a mean frequency $\bar{f}$ and a mean propagation direction $\bar{\theta}$, of bottom pressure energy within the frequency range 0.05–0.25 Hz, and the corresponding standard deviations σ_f and σ_θ are listed in table 1 (the details of the estimation technique are given in Appendix B). The observed $\bar{f}$ and σ_f range from 0.10–0.14 Hz and 0.03–0.04 Hz, respectively. Thus primary waves are most energetic in the frequency range 0.06–0.18 Hz and the dominant sum-frequency secondary wave contributions are expected in approximately the frequency range 0.12–0.36 Hz. The observed $|\bar{\theta}|$ are less than 5° and the σ_θ range from 12° to 19°, consistent with the expected refraction of long waves towards normal incidence.

3. Nonlinear theory for wave pressure and orbital velocities

The pressure and orbital velocity field of weakly nonlinear surface gravity waves in arbitrary water depth h can be derived through a perturbation expansion of the surface boundary conditions and Bernoulli equation (e.g. Hasselmann 1962; Hasselmann *et al.* 1963). The lowest order (primary) wave field is a frequency (σ)-directional (θ) spectrum of statistically independent free wave components with vector wavenumber $\boldsymbol{k} = [k\cos\theta, k\sin\theta]$ obeying the linear dispersion relation

$$\sigma = [gk\tanh(kh)]^{\frac{1}{2}}, \tag{1}$$

where g is the acceleration due to gravity and $\sigma = 2\pi f$. At the next order, secondary waves are generated in nonlinear triad interactions with two primary wave components. Each pair of primary (free) waves, with frequencies and wavenumbers $(\sigma_1, \boldsymbol{k}_1)$ and $(\sigma_2, \boldsymbol{k}_2)$, is accompanied by a pair of secondary waves with the sum $(\sigma_1+\sigma_2, \boldsymbol{k}_1+\boldsymbol{k}_2)$ and difference $(\sigma_1-\sigma_2, \boldsymbol{k}_1-\boldsymbol{k}_2$; for $\sigma_1 \geqslant \sigma_2$) frequency and wavenumber. Secondary waves are forced waves (frequently called 'bound' waves) with longer (sum interactions) or shorter (difference interactions) wavelengths than free surface waves (equation (1)) of the same frequency (e.g. Phillips 1960).

The present study is focused on sum-frequency secondary waves. To second order in non-linearity, at frequencies high enough that difference-frequency secondary waves are negligible, wave pressure p (normalized by ρg with ρ the density of sea

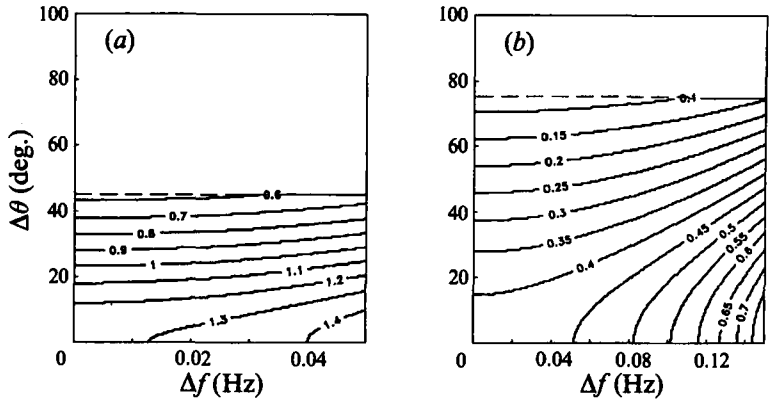

FIGURE 2. Theoretical values of the interaction coefficient D (equation (4)) as a function of the differences in frequency Δf and propagation direction $\Delta\theta$ of the primary wave components, for constant sum frequency f. (*a*) $f = 0.15$ Hz. (*b*) $f = 0.25$ Hz. The dashed curves indicate the maximum $\Delta\theta$ for a pair of primary waves incident from deep water on a gently sloping beach with parallel contours, (9).

water) and orbital velocities $\boldsymbol{u}(=[u,v,w])$ are given by (Hasselmann 1962; Hasselmann *et al.* 1963):

$$p = -\frac{1}{g}\left[\frac{\partial}{\partial t}\Phi^{(1)} + \frac{\partial}{\partial t}\Phi^{(2)} + \frac{[\nabla\Phi^{(1)}]^2}{2}\right], \tag{2a}$$

$$\boldsymbol{u} = \nabla\Phi^{(1)} + \nabla\Phi^{(2)}, \tag{2b}$$

where t is time and ∇ is the gradient operator. $\Phi^{(1)}$ and $\Phi^{(2)}$ are the primary and secondary velocity potential functions, respectively,

$$\Phi^{(1)}(t,\boldsymbol{x},z) = \int_{\boldsymbol{k}} \mathrm{d}Z(\boldsymbol{k}) \exp[\mathrm{i}(\boldsymbol{k}\cdot\boldsymbol{x} - \sigma t)] \frac{g\cosh(kz)}{\mathrm{i}\sigma} + \text{c.c.}, \tag{3a}$$

$$\Phi^{(2)}(t,\boldsymbol{x},z) = \int_{\boldsymbol{k}_1}\int_{\boldsymbol{k}_2} D(\boldsymbol{k}_1,\boldsymbol{k}_2)\,\mathrm{d}Z(\boldsymbol{k}_1)\,\mathrm{d}Z(\boldsymbol{k}_2) \exp[\mathrm{i}[(\boldsymbol{k}_1+\boldsymbol{k}_2)\cdot\boldsymbol{x} - (\sigma_1+\sigma_2)t]] \times \frac{g\cosh(|\boldsymbol{k}_1+\boldsymbol{k}_2|z)}{\mathrm{i}(\sigma_1+\sigma_2)} + \text{c.c.}, \tag{3b}$$

where $\mathrm{d}Z$ is the complex sea-floor pressure amplitude, $\boldsymbol{x}(=[x,y])$ is the horizontal space coordinate, z is the vertical elevation above the sea bed, σ and k are related by the dispersion relation (1), and c.c. is the complex conjugate of the right-hand side expression. D is the interaction coefficient

$$D(\boldsymbol{k}_1,\boldsymbol{k}_2) = \frac{\cosh(k_1 h)\cosh(k_2 h)}{M(\boldsymbol{k}_1,\boldsymbol{k}_2)\cosh(|\boldsymbol{k}_1+\boldsymbol{k}_2|h)} \times \left\{\frac{\sigma_1\sigma_2}{g} - \frac{g\boldsymbol{k}_1\cdot\boldsymbol{k}_2}{\sigma_1\sigma_2} - \frac{g}{2(\sigma_1+\sigma_2)}\left[\frac{k_1^2}{\sigma_1\cosh^2(k_1 h)} + \frac{k_2^2}{\sigma_2\cosh^2(k_2 h)}\right]\right\}, \tag{4}$$

where M is the relative mismatch of $(\sigma_1+\sigma_2, \boldsymbol{k}_1+\boldsymbol{k}_2)$ from the dispersion relation (1)

$$M(\boldsymbol{k}_1,\boldsymbol{k}_2) \equiv \frac{g|\boldsymbol{k}_1+\boldsymbol{k}_2|\tanh[|\boldsymbol{k}_1+\boldsymbol{k}_2|h] - (\sigma_1+\sigma_2)^2}{(\sigma_1+\sigma_2)^2}. \tag{5}$$

Secondary wave properties theoretically depend on the frequency-directional spectrum of primary waves which cannot be accurately estimated from the acoustic Doppler velocity measurements (Appendix B; Herbers & Guza 1990; Herbers *et al.*

1991). However, the present observations were obtained in relatively shallow water where (it is shown below) directional spreading effects on sum-frequency secondary waves are small.

For primary waves in shallow water ($k_1 h, k_2 h \ll 1$) the relative mismatch M is small (and the interaction coefficient D is large) when the waves are colinear ($\Delta\theta = 0$, where $\Delta\theta$ is the difference in propagation direction $|\theta_1 - \theta_2|$),

$$M(\boldsymbol{k}_1, \boldsymbol{k}_2) = (k_1 h)(k_2 h) + O(kh)^4; \quad \Delta\theta = 0. \tag{6}$$

Although M is not small when $\Delta\theta$ is large, $\Delta\theta$ is generally reduced in shallow water owing to refraction. On a mildly sloping beach with parallel contours, the free wave propagation direction θ relative to the beach normal is given by Snell's law

$$\theta = \arcsin\left[\tanh(kh)\sin(\theta_0)\right], \tag{7}$$

where θ_0 is the deep-water propagation direction. Substitution of (7) in the general expression (4) for the interaction coefficient $D(\boldsymbol{k}_1, \boldsymbol{k}_2)$ and expanding the result for small kh yields

$$D(\boldsymbol{k}_1, \boldsymbol{k}_2) = \frac{3g}{2\sigma_1 \sigma_2 h^2}\left\{\left(1 + \left[\frac{\sigma_1 \sin(\theta_{1,0}) - \sigma_2 \sin(\theta_{2,0})}{\sigma_1 + \sigma_2}\right]^2\right)^{-1} + O((kh)^2)\right\}, \tag{8}$$

where $\theta_{1,0}$ and $\theta_{2,0}$ are the deep-water propagation directions of wave components 1 and 2, respectively. When $\sigma_1 \approx \sigma_2$ the maximum value of $D = 3g/2\sigma_1\sigma_2 h^2$ for nearly colinear waves is reduced by only a factor of two for the extreme case of two primary waves arriving from opposite quadrants with grazing approach angles ($|\theta_{1,0} - \theta_{2,0}| = \pi$). In general the reduction of D is much less. The enhancement of sum-frequency secondary waves in shallow water depends only weakly on the details of the directional spectrum, consistent with numerical results based on the Boussinesq equations (Freilich, Guza & Elgar 1990).

The frequencies of the observed spectral maxima were between 0.06 and 0.14 Hz for which $0.3 < kh < 0.9$. Although (8) is not valid for the largest values of kh, the directional dependence of the interaction coefficient D is similarly weak. The theoretical maximum value of $\Delta\theta$ is from (7)

$$\Delta\theta_{\max} = \arcsin\left[\tanh(k_1 h)\right] + \arcsin\left[\tanh(k_2 h)\right]. \tag{9}$$

The dependence of D (for arbitrary kh, equation (4)), on the sum ($f = f_1 + f_2$) and difference ($\Delta f = |f_1 - f_2|$) frequencies of two primary wave components in 7 m depth, with $\Delta\theta < \Delta\theta_{\max}$, is shown in figure 2. The ranges of Δf correspond to primary wave frequencies higher than 0.05 Hz, and the sum frequencies f (0.15 and 0.25 Hz) are typical double swell frequencies. Significant reductions in D (and hence secondary wave energy) occur only for extremely broad directional spectra (i.e. $\Delta\theta$ close to $\Delta\theta_{\max}$) that are unusual at the present field site. Narrow directional spectra were observed (σ_θ ranges from 12°–19°, table 1), yielding values of D for typical $\Delta\theta$ that are well within about 20% of the values for colinear free wave interactions in the relevant frequency range (figure 2). Hence, sum-frequency secondary waves can in the present case be predicted fairly accurately from wave frequency spectra alone, neglecting the relatively weak directional spreading effects.

Hasselmann's weakly nonlinear theory is formally valid only for the irrotational wave motion above the wave bottom boundary layer, where the present velocity measurements were obtained. However, the pressure transducer was buried a few cm in the sand. The secondary pressure field includes contributions from both the secondary wave velocity potential ($\partial\Phi^{(2)}/\partial t$) and the local flow (the Bernoulli term $\frac{1}{2}(\nabla\Phi^{(1)})^2$) (equation 2($a$); Hasselmann *et al.* 1963; Cavaleri 1980). Turbulent

boundary layer effects on secondary wave pressure at the sea floor are not understood, but are expected to be small if the local flow is relatively weak (i.e. if $\frac{1}{2}(\nabla \Phi^{(1)})^2 \ll |\partial \Phi^{(2)}/\partial t|$), as occurs in shallow water where $\Phi^{(2)}$ is amplified by the small mismatch from resonance ((3*b*), (8)). The contribution of the local flow to the secondary bottom pressure field is $O(10\%)$ in the present observations (table 1) and pressure changes across the wave bottom boundary layer are assumed negligible.

4. Spectra of primary and secondary waves

For free surface gravity waves, the combined velocity spectrum

$$E_{\mathrm{vel}}(f) = E_u + E_v + 2E_w$$

(equation (A 1)) is related to the bottom pressure spectrum $E_p(f)$ ((2), 3(*a*) neglecting secondary wave contributions):

$$E_{\mathrm{vel}}(f) = G_l^2(f) E_p(f), \tag{10}$$

where $G_l(f) \equiv (gk/2\pi f)\ [1+3\sinh^2(kd)]^{\frac{1}{2}}$ and d is the height of the velocity measurements above the sea bed (2.5 m). Bottom pressure spectra, both directly observed and predicted from the velocity measurements with linear theory (10), on four occasions with rather different wave fields are shown in figure 3 (the following analysis of nonlinear effects is focused on these four cases). The observed velocity–pressure transfer function $G(f)$ (normalized by the theoretical linear transfer function G_l)

$$G(f) \equiv \frac{[E_{\mathrm{vel}}(f)/E_p(f)]^{\frac{1}{2}}}{G_l(f)} \tag{11}$$

is shown for all ten days in figure 4. The agreement between predicted and measured pressure is excellent in the energetic part of the spectrum (figure 3) with $G(f)$ typically within 1 ± 0.02 in the range 0.08–0.16 Hz and within 1 ± 0.1 in the range 0.05–0.25 Hz (figure 4). G_{tot}, where G_{tot}^2 is the ratio of predicted (from the velocity measurements, (10)) to observed pressure variance in the frequency range 0.05–0.25 Hz

$$G_{\mathrm{tot}} \equiv \left[\int_{0.05\,\mathrm{Hz}}^{0.25\,\mathrm{Hz}} \mathrm{d}f E_{\mathrm{vel}}(f)/G_l^2(f) \Big/ \int_{0.05\,\mathrm{Hz}}^{0.25\,\mathrm{Hz}} \mathrm{d}f E_p(f)\right]^{\frac{1}{2}} \tag{12}$$

is within 1 ± 0.02 for all 10 days (table 1), consistent with the dominance of free waves in the energetic part of the spectrum and the estimated accuracy of the pressure sensor calibration.

Sum-frequency forced waves reduce $G(f)$ because they have wavelengths longer than free waves of the same frequency, and the velocity/pressure amplitude ratio (for a fixed frequency) depends inversely on the wavelength. For frequencies between about 0.2 and 0.35 Hz the predicted pressure spectra diverge only slightly from the measured spectra (figure 3), with $G(f)$ generally less than 1 and decreasing as the frequency increases (figure 4). At frequencies higher than about 0.35 Hz, where dispersion is not weak ($kh > 1$), $G(f)$ is as small as 0.5, suggesting that relatively long-wavelength forced wave contributions are important at these high frequencies. At the lowest frequency band considered (0.05 Hz) the observed $G(f) > 1$ is qualitatively consistent with the theoretically expected contributions of relatively short-wavelength forced waves excited by difference-frequency interactions of swell and sea (e.g. Longuet-Higgins & Stewart 1962; Hasselmann 1962; Hasselmann *et al.* 1963). Deviations from linear theory are generally small when energy levels are low (e.g. 22 May, figure 3*d*) and tend to be larger with energetic swell (e.g. 8 April, figure

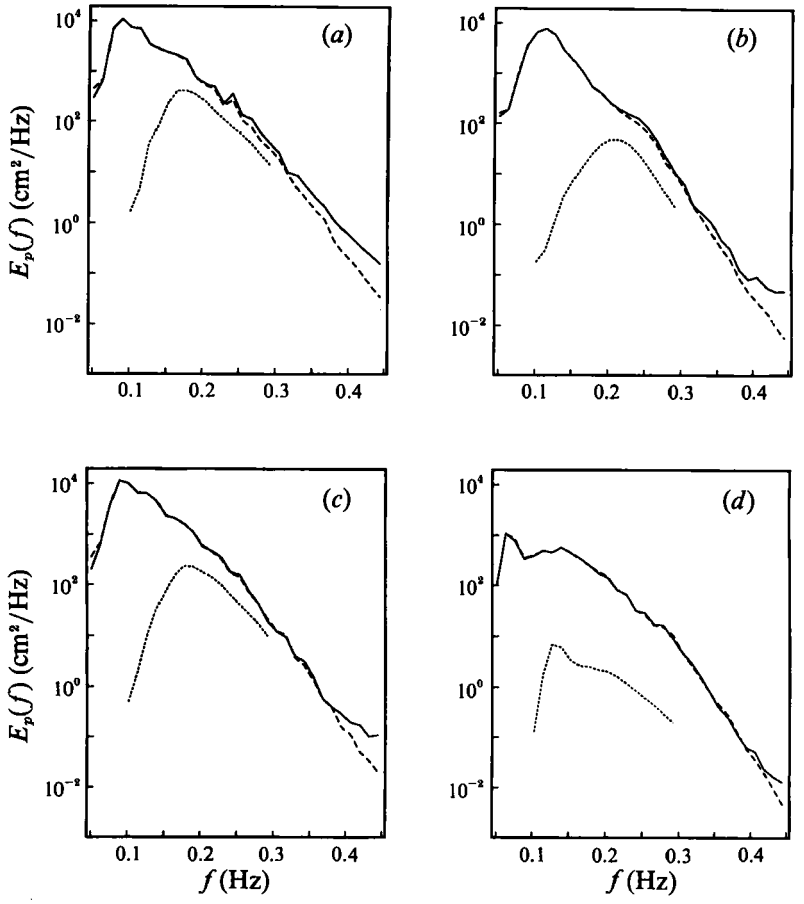

FIGURE 3. The directly measured bottom pressure spectrum $E_p(f)$ (solid), a prediction of $E_p(f)$ based on the velocity data and linear theory (dashed; see (10)), and a prediction of the secondary wave contribution $E_{p,\text{forced}}(f)$ to $E_p(f)$ (dotted; (14a)). (a) 8 April, (b) 10 April, (c) 10 May, (d) 22 May. The spectra have between 80 and 160 degrees of freedom.

3a), but this is not always the case (e.g. on 10 May when the bottom pressure variance was maximum, the observed $G(f)$ is very close to 1 for frequencies as high as 0.33 Hz; figures 3c, 4).

Figure 5 shows the observed ratio $H(f)$ between vertical and horizontal velocities, normalized by the theoretical value for free waves,

$$H(f) \equiv \left[\frac{1}{\tanh(kd)} + kR\left(1+\frac{1}{2\tanh^2(kd)}\right)\right]\left(\frac{E_{\hat{w}}(f)}{E_{\hat{u}}(f)+E_{\hat{v}}(f)}\right)^{\frac{1}{2}}. \tag{13}$$

A correction for the $O(kR)$ bias in velocity estimates (Appendix A (A 3)) is included in (13). On all ten days the observed $H(f)$ differ from linear theory by less than 10% over the frequency range 0.07–0.28 Hz. At low frequency the flow field is horizontally polarized and E_w is theoretically a small fraction of E_u+E_v (about 1% at 0.05 Hz). The degraded agreement of the observed $H(f)$ with linear theory below 0.07 Hz (figure 5) may thus be due to errors in the orientation of the instrument about vertical and the tilt of the sea bed (both about 1°).

The close agreement of the transfer functions G and H with linear theory in a wide frequency range, extending well beyond twice the spectral peak frequency, is perhaps

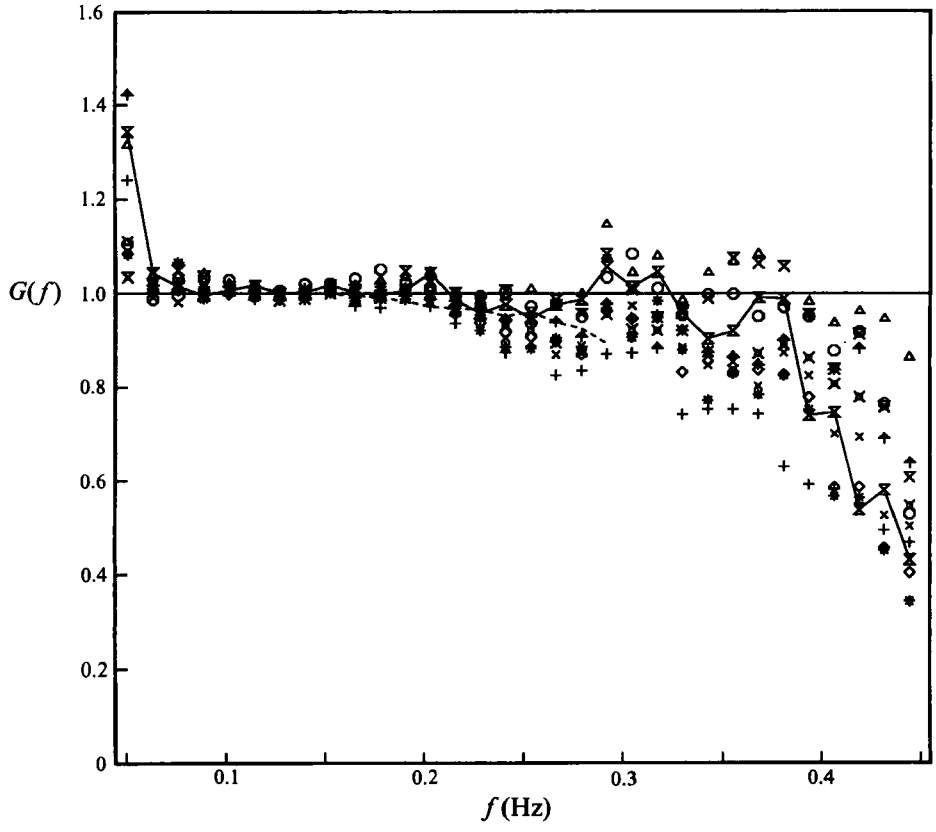

FIGURE 4. Estimates of the normalized transfer function $G(f)$ between velocity and pressure measurements (11) on all 10 days. Δ, 29 March; ○, 30 March; ◇, 3 April; +, 8 April; *, 10 April; ×, 29 April; ⋇, 30 April; ↑, 1 May; ⧖, 10 May; ⧗, 22 May. The solid and dashed curves are the observed and predicted (based on second-order nonlinear theory) $G(f)$, respectively, on 10 May.

somewhat surprising. For example, on 10 May the significant wave height was about 1.3 m ($4\eta_{\rm rms}$, table 1) and, based on the wave height to depth ratio, occasional breaking of the larger waves may have occurred (e.g. Thornton & Guza 1983). Yet the observed G and H differ by only a few percent from the theoretical linear value 1 at twice the spectral peak frequency (figures 3*c*, 4, 5). It is now shown that secondary wave contributions are indeed significant, but their effect on the transfer functions G and H is small.

In the present study the relatively weak directional spreading effects (§3) are neglected in predictions of secondary waves. For unidirectional primary waves, the theoretical contributions of sum-frequency secondary waves to the pressure ($E_{p,\,\rm forced}(f)$) and velocity ($E_{\rm vel,\,forced}(f)$) spectra are, from (2), (3),

$$E_{p,\,\rm forced}(f) = \int_0^f {\rm d}f' \left[D(k_{f'}, k_{f-f'}) - \frac{g k_{f'} k_{f-f'}}{8\pi^2 f'(f-f')}\right]^2 E_{p,\,\rm free}(f') E_{p,\,\rm free}(f-f'), \quad (14a)$$

$$E_{\rm vel,\,forced}(f) = \int_0^f {\rm d}f' D^2(k_{f'}, k_{f-f'}) \left(\frac{2\pi f'(f-f')(k_{f'}+k_{f-f'})}{g f k_{f'} k_{f-f'}}\right)^2$$

$$\times \frac{1+3\sinh^2[(k_{f'}+k_{f-f'})d]}{[1+3\sinh^2(k_{f'}d)][1+3\sinh^2(k_{f-f'}d)]} E_{\rm vel,\,free}(f') E_{\rm vel,\,free}(f-f'), \quad (14b)$$

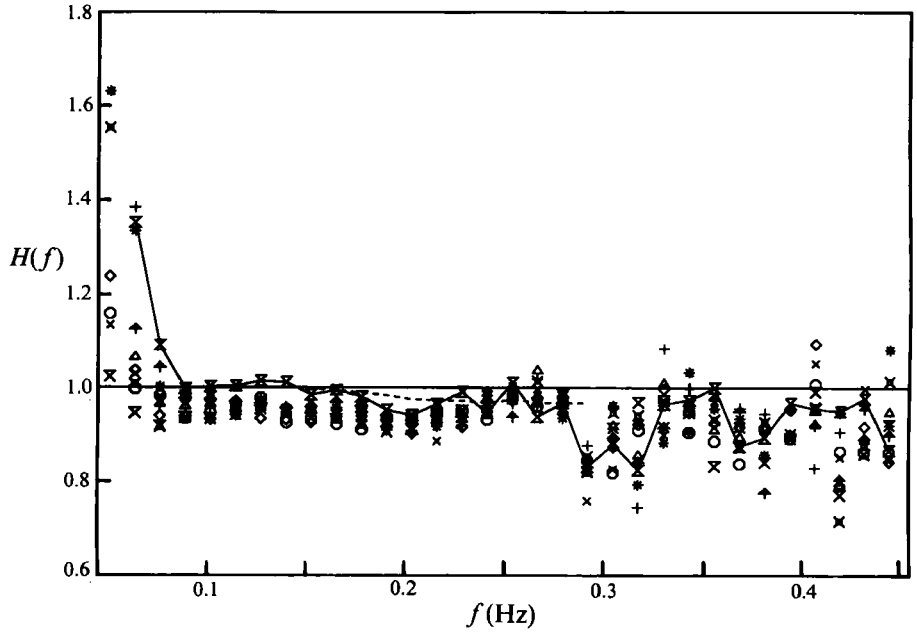

FIGURE 5. Estimates of the normalized transfer function $H(f)$ between the vertical and horizontal velocity components (13) on all 10 days. The solid and dashed curves are the observed and predicted (based on second-order nonlinear theory) $H(f)$, respectively, on 10 May. Symbols as figure 4.

where $D(k_1, k_2)$ is equal to $D(\boldsymbol{k}_1, \boldsymbol{k}_2)$ with $\boldsymbol{k}_1$ and $\boldsymbol{k}_2$ colinear, see (4), and $E_{p,\text{free}}$ and $E_{\text{vel,free}}$ are primary wave spectra.

Theoretical predictions of $E_{p,\text{forced}}(f)$ and $E_{\text{vel,forced}}(f)$ were obtained by substituting the measured pressure and velocity spectra, in the frequency range 0.05–0.25 Hz, in (14*a*) and (14*b*), respectively. Figure 3 shows $E_{p,\text{forced}}(f)$ predictions, in the double swell/sea frequency range 0.1–0.3 Hz, for four days selected to include cases ranging from negligible to moderately strong nonlinearity. Figure 6 shows the ratio between predicted (forced waves) and measured (free and forced waves) spectra, $E_{p,\text{forced}}(f)/E_p(f)$ and $E_{\text{vel,forced}}(f)/E_{\text{vel}}(f)$. In all cases (figure 6 and the days not shown) $E_{p,\text{forced}}/E_p$ and $E_{\text{vel,forced}}/E_{\text{vel}}$ are approximately equal as expected in relatively shallow water ($kh < 1$) where deviations of forced secondary waves from the linear dispersion curve are relatively small ($O(kh)^2$), and the linear (for free waves) and nonlinear (for forced waves) velocity–pressure ratios differ by only $O(kh)^2$ (see (2), (3), (6), (8)). The relative forced wave contributions at double swell and sea frequencies are small ($O(1\%)$) on 22 May when energy levels were low, but significant ($O(20$–$50\%)$) on the other three days with energetic swell (figures 3, 6 and table 1). The predicted forced wave energy (below 0.3 Hz) is driven primarily by interactions between spectral components within the most energetic part of the spectrum, typically 0.06–0.18 Hz (table 1, figure 3), where free waves are dominant (figure 6). Consequently, the predictions of secondary waves are insensitive both to the frequency (here 0.25 Hz) chosen as the maximum for free waves and to the inclusion of (relatively small) forced wave energy in the right-hand side of (14).

Predictions of the velocity–pressure ratio $G(f)$, (11), including forced secondary wave contributions, were calculated using the measured pressure spectrum to predict both $E_{p,\text{forced}}$ (14*a*), $E_{\text{vel,free}}$ ((10), substituting $E_p - E_{p,\text{forced}}$ for the pressure

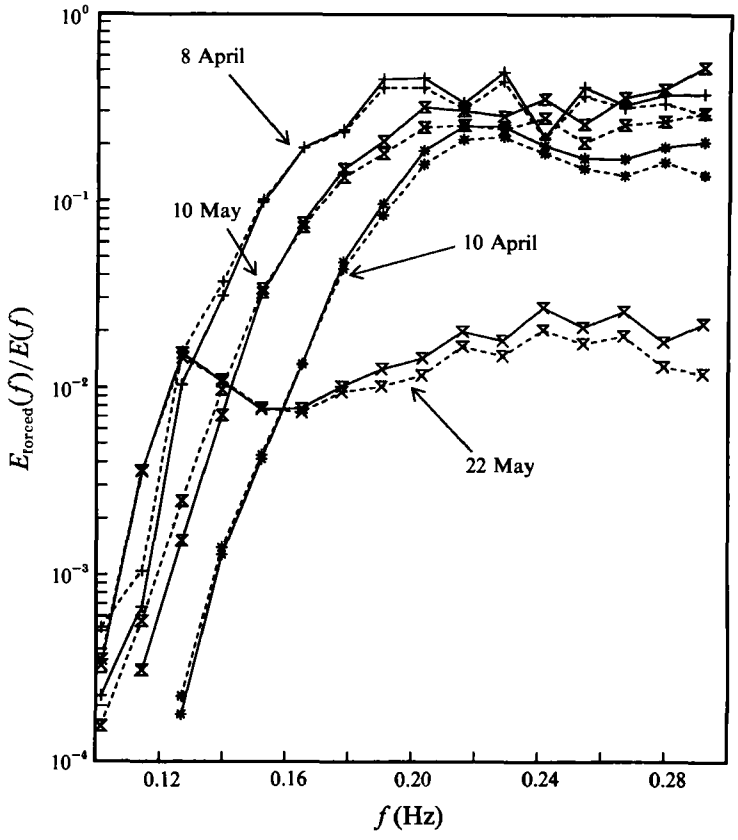

FIGURE 6. Ratio between predicted (forced secondary wave) and measured (free and forced wave) spectra of pressure (solid, (14*a*)) and velocity (dashed, (14*b*)) at double swell and sea frequencies on 8 April, 10 April, 10 May and 22 May, 1991 (the pressure spectra are shown in figure 3).

spectrum), and $E_{\text{vel, forced}}$ (14*b*). Similar predictions of $H(f)$ were obtained using the measured horizontal velocity spectra to estimate forced secondary wave contributions to $\hat{u}$, $\hat{v}$ and $\hat{w}$ spectra. Nonlinear predictions of $G(f)$ and $H(f)$ on 10 May show only small reductions from the theoretical value 1 for linear waves as observed (figures 4 and 5). The transfer functions G and H are insensitive to forced wave energy in shallow water and the good agreement (within 10%) with linear theory transfer functions at double swell frequencies (figures 4 and 5) is thus not inconsistent with the predicted relatively large (as much as 50%, figure 6) secondary wave energy levels.

In relatively shallow water ($kh < 1$) where the vertical decay of pressure is weak, the ratio α between root-mean-square forced (secondary) and free (primary) wave pressure

$$\alpha \equiv \frac{p_{\text{rms, forced}}}{p_{\text{rms, free}}} \approx \left[\int_{0.1\text{ Hz}}^{0.3\text{ Hz}} \mathrm{d}f E_{p,\text{forced}}(f) \Big/ \int_{0.05\text{ Hz}}^{0.25\text{ Hz}} \mathrm{d}f E_p(f) \right]^{\frac{1}{2}} \tag{15}$$

is essentially a bulk measure of the perturbation parameter in the expansion for weak nonlinearity. The parameter α fully incorporates the theoretical effects of wave slope, water depth and spectral shape on the nonlinearity of the wave field, as opposed to simpler metrics such as a characteristic wave slope based on the peak frequency and root-mean-square wave height. The estimates of α range from 0.05 to 0.22 (table

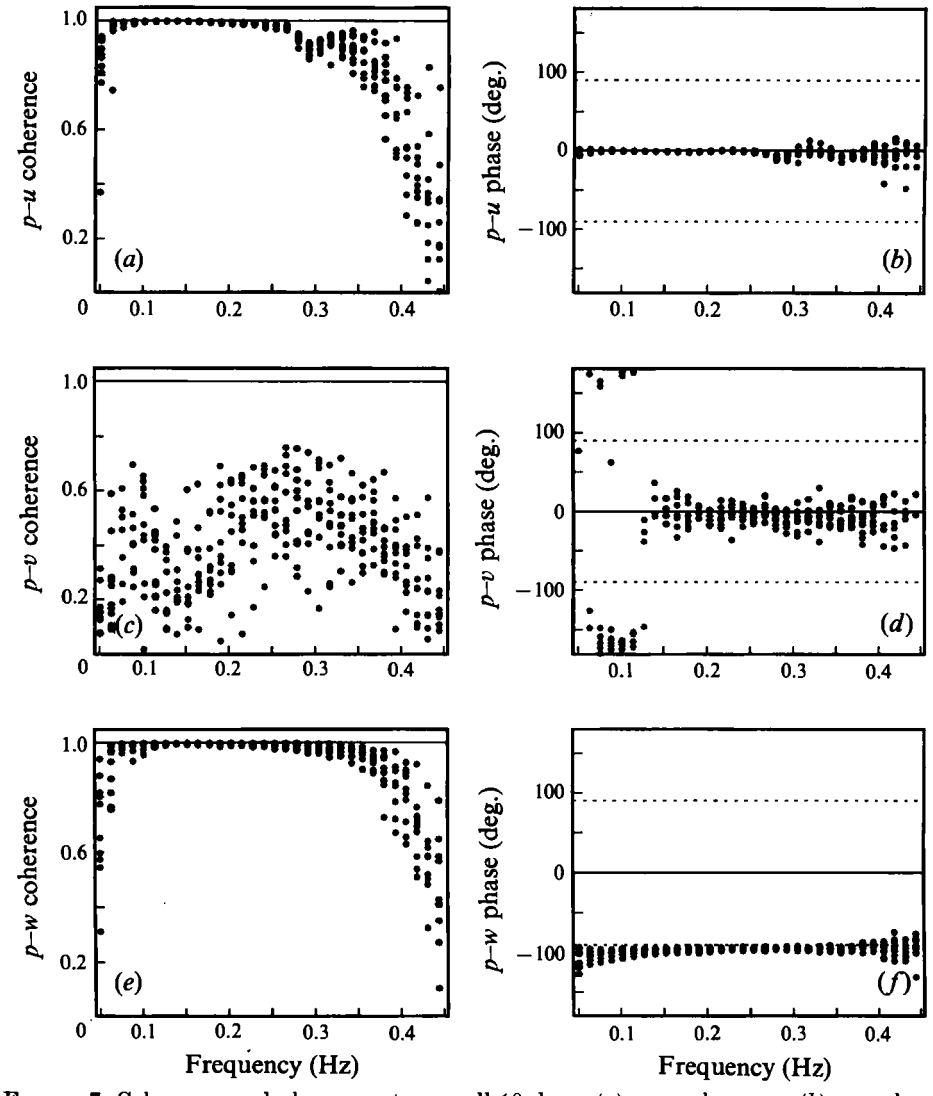

FIGURE 7. Coherence and phase spectra on all 10 days. (*a*) *p*–*u* coherence; (*b*) *p*–*u* phase; (*c*) *p*–*v* coherence; (*d*) *p*–*v* phase; (*e*) *p*–*w* coherence; (*f*) *p*–*w* phase. The 95% confidence level for zero coherence varies between 0.19 and 0.27.

1) and show that nonlinear effects are pronounced in cases when pressure–velocity transfer functions are within a few percent of the linear theory predictions.

According to linear theory, the coherence between p and w is equal to 1 independent of the directional distribution of energy, but the coherence between pressure and the horizontal velocity components may be significantly reduced by directional spreading effects. For primary waves, the theoretical phase spectra of p and u, and p and v are equal to 0° or 180° (depending on the direction of wave propagation) and the phase spectrum of p and w is always equal to $-90°$, (2), (3*a*). The same coherence and phase relationships theoretically hold for secondary wave contributions to the pressure and velocity measurements, (2), (3*b*), because in shallow water deviations of forced waves, from the free wave dispersion curve are small and the Bernoulli term in (2*a*) is negligible. The velocity gradients $\partial u/\partial z$, $\partial v/\partial z$

and $\partial w/\partial z$ have the same directional dependence and are in phase with u, v and w, respectively, (2*b*), (3), and thus the bias terms in $\hat{u}$, $\hat{v}$ and $\hat{w}$ (Appendix A, (A 3)) do not affect pressure–velocity phase estimates.

Figure 7 shows the coherence and phase spectra between p and the velocity estimates $\hat{u}$, $\hat{v}$ and $\hat{w}$. The observed coherence between p and the cross-shore component u (figure 7*a*) is always close to 1 for frequencies in the range 0.06–0.25 Hz, consistent with shoreward propagating waves refracted in relatively shallow water to near normal incidence. Above 0.25 Hz, the p–u coherence is slightly reduced, suggesting that directional spreading is significant. The p–u phase (figure 7*b*) is close to 0 in the entire frequency range 0.05–0.4 Hz, consistent with the theoretical phase relationship for shoreward propagating primary and secondary waves. The observed cross-spectra of pressure and the longshore velocity component v (figure 7*c*, *d*) show significant directional spreading effects on all ten days with low coherences and phases scattered about the theoretical values of 0° and 180° (waves arriving from the Northern and Southern quadrants, respectively). The p–w coherence and phase spectra (figure 7*e*, *f*) are close to the theoretical values 1 and −90° in a wide frequency range (0.07–0.35 Hz). The deviations of coherence and phase from the theoretical values at the lowest frequency band (0.05 Hz) possibly result from difference-frequency forced waves and (for w) sensor orientation errors.

5. Phase-coupling between primary and secondary waves

Natural wind-generated surface gravity waves have approximately Gaussian statistics owing to the statistical independence of primary wave components generated by independent wind forces on the sea surface. However, the amplitudes and phases of secondary and primary waves are not statistically independent but coupled through the interaction coefficient D, (3), (4), thus introducing non-Gaussian statistics.

Deviations from Gaussian statistics in the pressure and velocity records were examined with third-order spectra (bispectra). A general stationary process $\xi(t)$ (e.g. wave pressure and orbital velocities) can be expressed in terms of the Fourier–Stieltjes transform $\mathrm{d}\Xi(f)$

$$\xi(t) = \int_{-\infty}^{\infty} \mathrm{d}\Xi(f) \exp(2\pi i f t). \tag{16}$$

The (third-order) bispectrum $B(f_1,f_2)$ is defined analogous to the conventional (second-order) spectrum $E(f)$ (Hasselmann *et al.* 1963)

$$E(f)\,\mathrm{d}f \equiv 2\mathscr{E}\{\mathrm{d}\Xi(f)\,\mathrm{d}\Xi(-f)\}, \tag{17a}$$

$$B(f_1,f_2)\,\mathrm{d}f_1\,\mathrm{d}f_2 \equiv 2\mathscr{E}\{\mathrm{d}\Xi(f_1)\,\mathrm{d}\Xi(f_2)\,\mathrm{d}\Xi(-f_1-f_2)\}, \tag{17b}$$

where $\mathscr{E}\{\,\}$ denotes the expected value. The bispectrum vanishes for the lowest-order (Gaussian) primary waves. Triads of two primary components and a secondary component, with frequencies f_1,f_2 and f_1+f_2, contribute the leading-order terms in $B(f_1,f_2)$.

The normalized (by the spectral densities at the three interacting frequencies) bispectrum $b(f_1,f_2)$,

$$b(f_1,f_2) \equiv \frac{B(f_1,f_2)}{[E(f_1)\,E(f_2)\,E(f_1+f_2)]^{\frac{1}{2}}}, \tag{18}$$

is frequently used to identify dominant triads (e.g. Elgar & Guza 1985; Herbers &

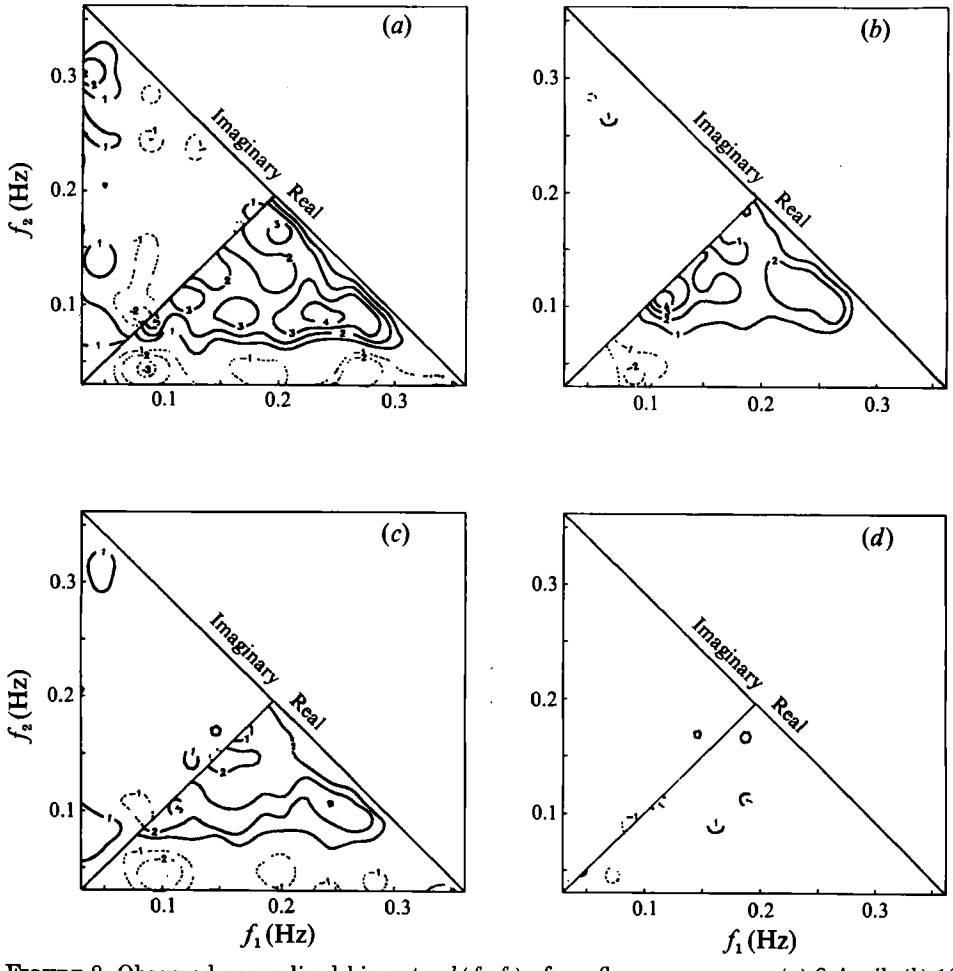

FIGURE 8. Observed normalized bispectra $b(f_1,f_2)$ of sea floor pressure on (*a*) 8 April, (*b*) 10 April, (*c*) 10 May and (*d*) 22 May, 1991. Contours (levels $\pm 1, 2, 3, 4$ Hz$^{-\frac{1}{2}}$) of the real and imaginary parts of the complex bispectrum b are shown in separate sectors as indicated. Solid and dotted contours indicate positive and negative values, respectively. The bispectra have between 120 and 240 degrees of freedom. The 95% confidence level for zero $|b(f_1,f_2)|$ varies between 1.1 and 1.6 Hz$^{-\frac{1}{2}}$.

Guza 1992; and others). The observed $b(f_1,f_2)$, (17), (18), of pressure on four occasions are shown in figure 8 (the corresponding spectra are shown in figure 3). On 22 May, when surface wave energy levels are low (figure 3*d*, table 1), the observed bispectral levels (figure 8*d*) are much smaller than in the other cases (figure 8*a–c*), consistent with the predicted relatively small secondary wave contributions at double swell and sea frequencies (figure 6). In this case, statistically independent primary waves dominate the pressure and velocity field at all frequencies between 0.04 and 0.36 Hz. On the other three days (when secondary wave energy levels are higher, figures 3*a–c* and 6) phase-coupling between energetic swell and higher-frequency forced waves is evident in the bispectra. On 10 April (figure 8*b*) the pressure bispectrum is maximum for $f_1 \approx f_2 \approx 0.12$ Hz, corresponding to the interactions between the primary 0.12 Hz swell peak and double swell frequency (≈ 0.24 Hz) secondary waves. The observed bispectral values are real (i.e. the imaginary part is close to zero) and positive for $f_1,f_2 > 0.07$ Hz, consistent with the theoretical phase relationship between primary and sum-frequency secondary waves (Hasselmann *et al.* 1963). The negative, real

bispectral values observed at lower frequencies are consistent with theoretically expected difference-frequency forced waves (e.g. Hasselmann *et al.* 1963; Okihiro, Guza & Seymour 1992; Elgar *et al.* 1992). On 8 April and 10 May, when the pressure (and surface elevation) variance and the nonlinearity parameter α, (15), are maximum (table 1), the real part of the observed pressure bispectrum also shows the theoretically expected positive values for sum interactions and negative values for difference interactions. However, in contrast to 10 April, the observed bispectra (in particular on 8 April) have statistically significant imaginary parts. This suggests that Hasselmann's weakly nonlinear theory is breaking down when the wave field is predicted to have the greatest nonlinearity (the bulk nonlinear perturbation parameter $\alpha = 0.22$ on 8 April, table 1). Previous observations (Elgar & Guza 1985) show that the imaginary part of the bispectrum increases as waves pitch forward during shoaling into even shallower (i.e. 2 m) depths.

At double swell frequencies (0.1–0.3 Hz) the expected dominant nonlinear effects are secondary wave components, forced by sum-frequency interactions between directionally narrow, nearly normally incident primary waves (table 1). Approximating the primary waves as colinear (as in (14)) the predicted velocity bispectra $B_{\hat{u}}$ and $B_{\hat{w}}$ are ((2)–(5))

$$B_{\hat{u}}(f_1,f_2) \approx D(k_1,k_2)E_{\hat{u},\mathrm{free}}(f_1)E_{\hat{u},\mathrm{free}}(f_2)\frac{2\pi f_1 f_2(k_1+k_2)}{g(f_1+f_2)k_1k_2}$$
$$\times[1+R((k_1+k_2)\tanh[(k_1+k_2)d]-k_1\tanh[k_1d]-k_2\tanh[k_2d])]. \quad (19a)$$

$$B_{\hat{w}}(f_1,f_2) \approx D(k_1,k_2)E_{\hat{w},\mathrm{free}}(f_1)E_{\hat{w},\mathrm{free}}(f_2)\frac{\mathrm{i}2\pi f_1 f_2(k_1+k_2)\tanh[(k_1+k_2)d]}{g(f_1+f_2)k_1k_2\tanh[k_1d]\tanh[k_2d]}$$
$$\times\left[1+\frac{R}{2}\left(\frac{k_1}{\tanh[k_1d]}+\frac{k_2}{\tanh[k_2d]}-\frac{k_1+k_2}{\tanh[(k_1+k_2)d]}\right)\right], \quad (19b)$$

where the terms enclosed in square brackets contain a correction for the $O(kR)$ bias in the velocity measurements (Appendix A, (A 3*a*, *c*)).

The observed, (17), (18), and predicted ((18) with B based on (19) and the measured velocity spectra) $\hat{u}$ and $\hat{w}$ normalized bispectra on 10 April (moderate swell energy and α, figure 3*b* and table 1) are compared in figure 9. The predictions are shown for the range of energetic sum-frequency triad interactions

$$(f_1+f_2 = 0.15\text{–}0.3\ \mathrm{Hz}, f_1,f_2 > 0.06\ \mathrm{Hz}).$$

The predicted bispectrum of $\hat{u}$ (similar to the bispectrum of p) is real, (19*a*), and the bispectrum of $\hat{w}$ (w is out of phase with p and u) is imaginary, (19*b*). The observed velocity bispectra (figure 9 and the days not shown) are generally consistent with these theoretical phase relationships. An exception is 8 April, when the departure of the phases of the $\hat{u}$ and $\hat{w}$ bispectra (not shown) from theory is similar to the deviations in the pressure bispectrum on this day (figure 8*a*).

The observed $b(f_1,f_2)$ of p, $\hat{u}$ and $\hat{w}$ are generally maximum at frequencies f_1,f_2 approximately equal to the spectral peak frequency, in good agreement with the predicted interactions between energetic swell components and double-swell-frequency secondary waves (e.g. figure 9). However, the observed large positive values of $b(f_1,f_2)$ at higher frequencies ($f_1+f_2 > 0.3$ Hz; e.g. figures 8*a–c*, and 9*c*, *d*) suggest that higher-order (tertiary, quarternary, ...) forced waves may be important. In particular on 8 April (figure 8*a*) the normalized bispectrum maximum at $f_1 \approx 0.24$ Hz, $f_2 \approx 0.08$ Hz could be the result of triad interactions between 0.08 Hz

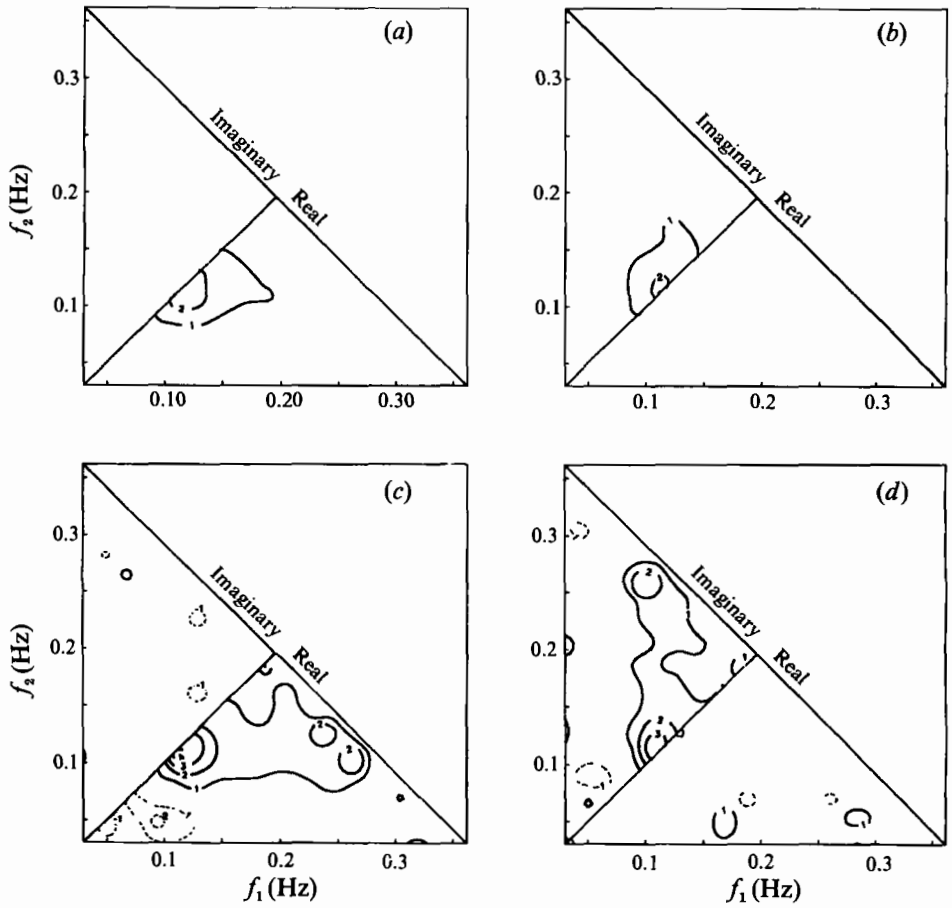

FIGURE 9. Observed (c, d) and predicted (a, b) normalized bispectra ($b(f_1,f_2)$, (18)) of the horizontal velocity component $\hat{u}(a,c)$ and the vertical velocity component $\hat{w}(b,d)$ on 10 April, 1991; contour plots have the same format as figure 8.

swell, 0.24 Hz seas and sum-frequency (0.32 Hz) secondary waves, or due to (0.08, 0.08, 0.08, 0.08, −0.32 Hz) quintet interactions which yield a 'Stokes-type' fourth harmonic of the 0.08 Hz swell peak. Bispectral analysis cannot resolve this question; higher-order spectra are required.

In general the surface wave field at double swell frequencies contains a mix of free (statistically independent) wind-generated seas and phase-coupled secondary waves. The relative contribution of secondary waves to the energy at frequency f is approximately given by integrating the bispectrum over all possible $(f',f-f',f)$ triads that force secondary waves with frequency f. Normalized by the second-order spectrum analogous to (18), the integrated bispectrum $b_i(f)$ is defined (Herbers & Guza 1992)

$$b_i(f) \equiv \int_0^f \mathrm{d}f' B(f-f',f') \Big/ \left[\int_0^f \mathrm{d}f' E(f-f') E(f') E(f)\right]^{\frac{1}{2}}. \tag{20}$$

For the observed narrow (both in direction and frequency, table 1) surface wave spectra, $|b_i(f)|^2$ at double swell frequencies (where contributions from difference-

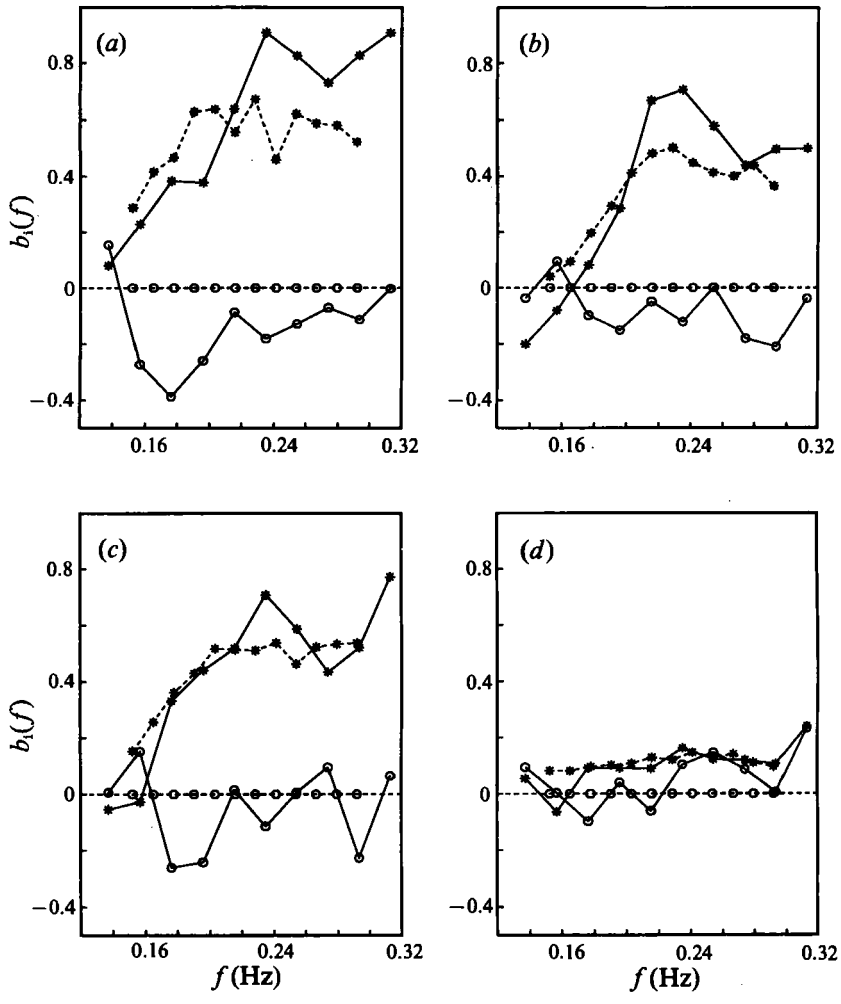

FIGURE 10. Observed (solid) and predicted (dashed) bispectra integrated for constant sum frequency $b_i(f)$ (20) of the horizontal velocity component $\hat{u}$, on (*a*) 8 April, (*b*) 10 April, (*c*) 10 May and (*d*) 22 May, 1991. Asterisks and circles denote the real and imaginary parts of $b_i(f)$, respectively.

frequency interactions and higher-order forced waves are relatively small) is approximately the fraction of the total energy at frequency f contributed by forced secondary waves (Herbers & Guza 1992). Observed ((17) and (20)) and predicted (substituting the measured spectra at frequencies 0.06–0.25 Hz for $E(f)$ in (19) and (20)) integrated velocity bispectra are compared in figures 10 ($\hat{u}$) and 11 ($\hat{w}$) on the same four occasions as shown in figures 3 and 8. The observed and predicted $|b_i|$ are small, $O(0.1)$, on 22 May when free waves dominate at all frequencies (figure 3*d*), and much larger (0.5–1) on the other three days, confirming that forced secondary waves contribute significantly to the high-frequency velocity field observed during energetic swell conditions. On 8 April, when predicted secondary wave energy levels were maximum (α in table 1), the real and imaginary parts of the observed $b_i(f)$ are comparable in magnitude at double swell frequencies (figures 10*a*, 11*a*; $f \approx 0.16$ Hz), indicating a significant departure from Hasselmann's weakly nonlinear theory (i.e., the waves are pitched forward as well as peaky). On the other days (including those

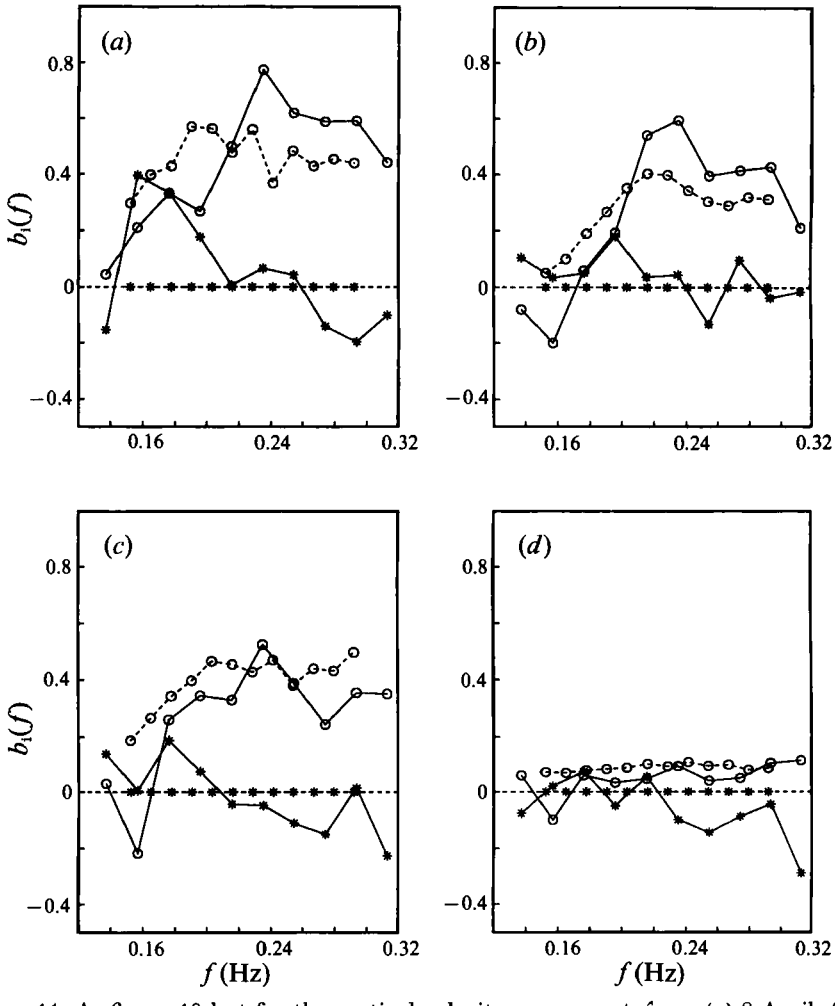

FIGURE 11. As figure 10 but for the vertical velocity component $\hat{w}$, on (*a*) 8 April, (*b*) 10 April, (*c*) 10 May and (*d*) 22 May, 1991.

not shown in figures 10 and 11) the observed imaginary part of the (integrated) $\hat{u}$ bispectrum and real part of the (integrated) $\hat{w}$ bispectrum are generally small, scattered approximately randomly about the theoretical value zero. Overall, the observed and predicted integrated bispectra are in good agreement, confirming that nonlinear effects on the wave orbital velocity field are accurately predicted by Hasselmann's (1962) theory even for relatively large values of the nonlinear perturbation parameter ($O(0.1$–$0.2)$, table 1).

6. Conclusions

Field measurements of wave orbital velocities and pressure, collected in the lower part of the water column in 7 m depth, are compared to the general second-order theory for weakly nonlinear surface gravity waves (Hasselmann 1962). Three-component (cross-shore u, longshore v and vertical w) velocity measurements at an elevation of 2.5 m above the sea bed were obtained with an acoustic Doppler current meter (figure 1). Pressure data were acquired with a co-located pressure transducer

buried a few cm below the sea bed. Wave energies (table 1) ranged from so low that forced waves are too small in amplitude to be detected in background free waves (i.e. high-frequency seas), to moderately high when strong nonlinearities cause significant departures from Hasselmann's weakly nonlinear theory.

Velocity and pressure measurements in the energetic part of the spectra are in excellent agreement with the theoretical linear transfer functions for free surface gravity waves (figures 3, 4). The observed and predicted (from the velocity measurements and linear theory) root-mean-square pressure fluctuations typically differ by less than 1%, independent of the swell energy (G_{tot} in table 1). The phase spectra between pressure and velocity measurements and the observed transfer function between vertical and horizontal velocity components also agree well with linear theory (figures 5, 7). These results confirm that the wavenumbers of the lowest-order primary waves are given to a high degree of accuracy by the linear dispersion relation.

Theoretical predictions of forced secondary wave statistics in principle require detailed directional information not provided by the pressure and velocity measurements. However, sum-frequency secondary wave properties are insensitive to the details of the narrow (owing to refraction) directional spectra occurring in shallow water (figure 2). Estimates of bulk directional properties verify that directional spreading effects are indeed small in the present observations, and secondary wave statistics can thus be predicted fairly accurately from the observed frequency spectra alone. On several occasions (e.g. figure 3*a–c*) the pressure and velocity spectra at double swell and sea frequencies theoretically contain a mix of about equal amounts of free and forced wave energy (figure 6). The ratio between the root-mean-square values of secondary and primary pressure fluctuations (a bulk average measure of the nonlinear perturbation parameter) varies from 0.05 to 0.22 (α in table 1). These theoretically predicted significant nonlinearities are obscured in the pressure–velocity transfer functions because the wavenumbers of forced waves are only slightly different from the wavenumbers of free waves with the same frequency.

Although nonlinearities have relatively little effect on pressure–velocity transfer functions in shallow water, Hasselmann's (1962) theory predicts large deviations from Gaussian statistics owing to phase-coupling between primary and secondary wave components. The observed magnitudes and phases of the pressure and velocity bispectra are generally consistent with the theoretical predictions (e.g. figures 8, 9). Good agreement between observed and predicted bulk integrals of the bispectrum confirms that the contribution of forced secondary waves to the energy at double swell frequencies is relatively small ($O(1\%)$) with low-energy swell (e.g. figures 10*d*, 11*d*) and significant ($O(20\text{–}50\%)$) with energetic swell (e.g. figures 10*a–c*, 11*a–c*). The observed phases of velocity and pressure bispectra show deviations from the theoretical values when secondary wave energy levels are maximum, indicating a breakdown of Hasselmann's theory (figures 8*a*, 10*a*, 11*a*).

This research was sponsored by the Office of Naval Research Coastal Sciences program. T.H.C.H. received additional support from the Office of Naval Research Geology and Geophysics program. The staff of the Center for Coastal Studies (Scripps Institution of Oceanography) built, installed and maintained the instruments.

Appendix A. Acoustic Doppler velocimeter

The X_+, X_-, Y_+ and Y_- beam pairs measure $(u+w)/\sqrt{2}$, $(-u+w)/\sqrt{2}$, $(v+w)/\sqrt{2}$ and $(-v+w)/\sqrt{2}$, respectively, at a distance $R = 0.71$ m from the instrument axis (figure 1). The sum of the velocity spectra $E_{X_+}(f)$, $E_{X_-}(f)$, $E_{Y_+}(f)$, and $E_{Y_-}(f)$ yields

$$E_{\rm vel}(f) \equiv E_{X_+}(f)+E_{X_-}(f)+E_{Y_+}(f)+E_{Y_-}(f) = E_u(f)+E_v(f)+2E_w(f), \quad \text{(A 1)}$$

where E_u, E_v and E_w are the spectra of the cross-shore, alongshore and vertical velocity components, respectively (for weakly nonlinear surface gravity waves the velocity co-spectra C_{uw} and C_{vw} vanish; e.g. Hasselmann 1962). By expanding the wave orbital velocity field about the vertical instrument axis, the sums and differences of the four beam measurements can be expressed in terms of u, v and w and their horizontal derivatives at a single location (Herbers *et al.* 1991)

$$X_{\rm dif} \equiv (X_+-X_-)/\sqrt{2} = u+R(\partial/\partial x)\,w+\tfrac{1}{2}R^2(\partial^2/\partial x^2)u+\tfrac{1}{6}R^3(\partial^3/\partial x^3)w+\ldots, \quad \text{(A 2}a\text{)}$$

$$Y_{\rm dif} \equiv (Y_+-Y_-)/\sqrt{2} = v+R(\partial/\partial y)w+\tfrac{1}{2}R^2(\partial^2/\partial y^2)v+\tfrac{1}{6}R^3(\partial^3/\partial y^3)w+\ldots, \quad \text{(A 2}b\text{)}$$

$$X_{\rm sum} \equiv (X_++X_-)/\sqrt{2} = w+R(\partial/\partial x)u+\tfrac{1}{2}R^2(\partial^2/\partial x^2)w+\tfrac{1}{6}R^3(\partial^3/\partial x^3)u+\ldots, \quad \text{(A 2}c\text{)}$$

$$Y_{\rm sum} \equiv (Y_++Y_-)/\sqrt{2} = w+R(\partial/\partial y)v+\tfrac{1}{2}R^2(\partial^2/\partial y^2)w+\tfrac{1}{6}R^3(\partial^3/\partial y^3)v+\ldots. \quad \text{(A 2}d\text{)}$$

The beam sums and differences can be combined to yield velocity estimates $\hat{u}$, $\hat{v}$ and $\hat{w}$ ((A 2) and assuming incompressible, irrotational flow)

$$\hat{u} \equiv X_{\rm dif} = u+R(\partial/\partial z)\,u+O(kR)^2, \quad \hat{v} \equiv Y_{\rm dif} = v+R(\partial/\partial z)\,v+O(kR)^2, \quad \text{(A 3}a, b\text{)}$$

$$\hat{w} \equiv \tfrac{1}{2}(X_{\rm sum}+Y_{\rm sum}) = w-\tfrac{1}{2}R(\partial/\partial z)w+O(kR)^2, \quad \text{(A 3}c\text{)}$$

with $(O(kR))$ bias errors (the second term on the right-hand side of (A 3)) owing to velocity changes over the finite separation of the sample volumes ((A 2); Herbers *et al.* 1991). This bias is taken completely into account in comparisons of observations and theoretical predictions of both primary and secondary waves. Higher-order $(O(kR)^2)$ bias errors in the velocity estimates are negligibly small for the wavelengths expected theoretically (less than 10% for primary and secondary waves with frequencies less than 0.4 Hz). Note that unlike (A 3), (A 1) is not based on an expansion for small kR and thus holds for all wavelengths that are long compared to the 40 cm horizontal span of the sample volumes (Herbers *et al.* 1991).

A significant source of measurement errors in the velocity data presented in Herbers *et al.* (1991) was interference from the sea surface. Sidelobes of the acoustic beams reaching the surface only have about 10^{-4} of the energy of the main lobe but their strong reflectivity from the sea surface interface yields an acoustic Doppler return that is nevertheless strong enough to seriously contaminate the relatively weak sound backscattered from the sample volumes. In the original acoustic Doppler instrument, acoustic pulses with a 1 ms duration were transmitted every 5 ms, and the arrival of backscattered sound sometimes coincided with the arrival of (sidelobe) reflections of the previous pulse from the sea surface (about 5 m above the sample volumes). To reduce the surface interference the timing of acoustic pulses was modified such that the arrivals of sound backscattered from the sample volumes and reflections of sidelobes from the sea surface do not coincide. In the present instrument, two pulses of sound energy with a 1 ms duration and separated by 2.5 ms are transmitted at 10 ms intervals. The 2.5 ms between a pair of pulses is short enough that the backscattered sound of the second pulse arrives at the receivers before surface reflections of the first pulse arrive. On the other hand, the 7.5 ms gap

following a pair of pulses is long enough that their surface reflections have arrived at the receivers well before the backscattered sound of the next pulse arrives. Thus the effect of surface interference is effectively eliminated, but only for depths conservatively estimated to range from about 6–8 m. The present data were collected at tidal stages when depth variations (including wave excursions) were within this range.

The coherent processing scheme (Lhermitte 1985) applied to the acoustic Doppler data has the advantage (over incoherent processing) of relatively low noise levels but yields aliased velocity data. The coherent processing used in this study uses both the pulse pairs separated by 2.5 ms and the pulse pairs separated by 7.5 ms. The latter yield more accurate (by virtue of a higher signal to noise ratio) but highly aliased (first aliases occur at ± 5 cm/s) velocity estimates. The present velocity data are based on Doppler frequency estimates of the 7.5 ms pulse pairs, using the Doppler frequency estimates of the 2.5 ms pulse pairs (first aliases occur at ± 15 cm/s) and a simple dealiasing algorithm to resolve the ambiguity.

Velocity spectra generally show a noise floor (at very high frequencies, > 1 Hz) of about 0.05 $(\mathrm{cm/s})^2/\mathrm{Hz}$, slightly lower than the 0.1 $(\mathrm{cm/s})^2/\mathrm{Hz}$ level in the acoustic Doppler data presented in Herbers *et al.* (1991; also based on coherent processing) and considerably lower than the 1 $(\mathrm{cm/s})^2/\mathrm{Hz}$ noise levels reported for electromagnetic current meters (Guza *et al.* 1988) used in previous studies.

Appendix B. Estimation of directional spreading effects

The acoustic Doppler measurements can provide low-resolution directional wave data equivalent to commonly used pitch-and-roll buoys and compact pressure sensor arrays (Herbers *et al.* 1991). The first four Fourier coefficients a_1, b_1, a_2 and b_2 of the directional distribution of free wave energy $S(\theta;f)$ at frequency f,

$$a_n(f) \equiv \langle \cos(n\theta) \rangle, \quad b_n(f) \equiv \langle \sin(n\theta) \rangle \tag{B 1a, b}$$

with

$$\langle y(\theta) \rangle \equiv \int_0^{2\pi} \mathrm{d}\theta\, y(\theta) S(\theta;f) \tag{B 2}$$

and $\theta = 0$ corresponding to normally incident shoreward propagating waves, can be expressed in terms of the co-spectra of the velocity ($\hat{u}$ and $\hat{v}$) and pressure (p) measurements, (2), (3a),

$$a_1(f) = \frac{C_{p\hat{u}}(f)}{(C_{pp}(f)[C_{\hat{u}\hat{u}}(f)+C_{\hat{v}\hat{v}}(f)])^{\frac{1}{2}}} + O(kR)^2,$$

$$b_1(f) = \frac{C_{p\hat{v}}(f)}{(C_{pp}(f)[C_{\hat{u}\hat{u}}(f)+C_{\hat{v}\hat{v}}(f)])^{\frac{1}{2}}} + O(kR)^2, \tag{B 3a, b}$$

$$a_2(f) = \frac{C_{\hat{u}\hat{u}}(f)-C_{\hat{v}\hat{v}}(f)}{C_{\hat{u}\hat{u}}(f)+C_{\hat{v}\hat{v}}(f)} + O(kR)^2, \quad b_2(f) = \frac{2C_{\hat{u}\hat{v}}(f)}{C_{\hat{u}\hat{u}}(f)+C_{\hat{v}\hat{v}}(f)} + O(kR)^2, \tag{B 3c, d}$$

where C_{ij} denotes the co-spectrum between measurements i and j and the $O(kR)^2$ bias is negligibly small (Appendix A; Herbers *et al.* 1991).

Directional spectra of surface gravity waves at the experiment site are expected to be relatively narrow ($|\theta| < \frac{1}{3}\pi$) owing to refraction of long-wavelength swell, limited fetches for wind waves with large oblique angles of incidence, and weak reflection

from the gently sloping beach. Hence a mean wave direction $\bar{\theta}$ and angular spread σ_θ defined as

$$\bar{\theta}(f) \equiv \langle\theta\rangle, \quad \sigma_\theta(f) \equiv [\langle\theta^2\rangle - \langle\theta\rangle^2]^{\frac{1}{2}} \tag{B 4a, b}$$

can be accurately expressed in terms of a_1, b_1, a_2 and b_2 by expanding (B 1) for small θ (e.g. Longuet-Higgins, Cartwright & Smith 1963; Kuik, van Vledder & Holthuijsen 1988)

$$\tfrac{4}{3}b_1(f) - \tfrac{1}{6}b_2(f) = \langle\theta[1 - \tfrac{1}{30}\theta^4 + O(\theta^6)]\rangle, \tag{B 5a}$$

$$\tfrac{5}{2} - \tfrac{8}{3}a_1(f) + \tfrac{1}{6}a_2(f) = \langle\theta^2[1 - \tfrac{1}{90}\theta^4 + O(\theta^6)]\rangle. \tag{B 5b}$$

The leading ($O(\theta^4)$) bias terms in (B 5) are very small (less than a few percent for $|\theta| < 60°$). The accuracy of $\bar{\theta}(f)$ and $\sigma_\theta(f)$ estimates based on (B 5) were verified by agreement with estimates based on a_1 and b_1 only ($\langle\theta\rangle \approx b_1(f)$, $\langle\theta^2\rangle \approx 2[1 - a_1(f)]$) and by agreement with estimates based on a_2 and b_2 only ($\langle\theta\rangle \approx \frac{1}{2}b_2(f)$, $\langle\theta^2\rangle \approx \frac{1}{2}[1 - a_2(f)]$).

REFERENCES

Battjes, J. A. & Heteren, J. van 1984 Verification of linear theory for particle velocities in wind waves based on field measurements. *Appl. Ocean Res.* **6**, 187–196.

Bowden, K. F. & White, R. A. 1966 Measurements of the orbital velocities of sea waves and their use in determining the directional spectrum. *Geophys. J. R. Astron. Soc.* **12**, 33–54.

Cavaleri, L. 1980 Wave measurement using pressure transducer. *Oceanol. Acta* **3**, 339–346.

Cox, C. S. & Jacobs, D. C. 1989 Cartesian diver observations of double frequency pressure fluctuations in the upper levels of the ocean. *Geophys. Res. Lett.*, **16**, 807–810.

Donelan, M. A., Hamilton, J. & Hui, W. H. 1985 Directional spectra of wind-generated waves. *Phil. Trans. R. Soc. Lond.* A **315**, 509–562.

Elgar, S., Freilich, M. H. & Guza, R. T. 1990 Model-data comparisons of moments of non-breaking shoaling surface gravity waves. *J. Geophys. Res.* **95**, 16055–16063.

Elgar, S. & Guza, R. T. 1985 Observations of bispectra of shoaling surface gravity waves. *J. Fluid Mech.* **161**, 425–448.

Elgar, S., Herbers, T. H. C., Okihiro, M., Oltman-Shay, J. & Guza, R. T. 1992 Observations of infragravity waves. *J. Geophys. Res.* (in press).

Freilich, M. H. & Guza, R. T. 1984 Nonlinear effects on shoaling surface gravity waves. *Phil. Trans. R. Soc. Lond.* A **311**, 1–41.

Freilich, M. H., Guza, R. T. & Elgar, S. L. 1990 Observations of nonlinear effects in directional spectra of shoaling gravity waves. *J. Geophys. Res.* **95**, 9645–9656.

Grimshaw, R. 1970 The solitary wave in water of variable depth. *J. Fluid Mech.* **42**, 639–656.

Guza, R. T., Clifton, M. C. & Rezvani, F. 1988 Field intercomparisons of electromagnetic current meters. *J. Geophys. Res.* **93**, 9302–9314.

Guza, R. T. & Thornton, E. B. 1980 Local and shoaled comparisons of sea surface elevations, pressures, and velocities. *J. Geophys. Res.* **85**, 1524–1530.

Guza, R. T. & Thornton, E. B. 1985 Velocity moments in nearshore. *J. Waterways, Port, Coastal Ocean Engng* **111**, 235–256.

Hasselmann, K. 1962 On the non-linear energy transfer in a gravity-wave spectrum. Part 1. General theory. *J. Fluid Mech.* **12**, 481–500.

Hasselmann, K, Munk, W. & MacDonald, G. 1963 Bispectra of ocean waves. In *Times Series Analysis* (ed M. Rosenblatt), pp. 125–139. John Wiley.

Herbers, T. H. C. & Guza, R. T. 1990 Estimation of directional wave spectra from multicomponent observations. *J. Phys. Oceanogr.* **20**, 1703–1724.

Herbers, T. H. C. & Guza, R. T. 1991 Wind-wave nonlinearity observed at the sea floor. Part I Forced wave energy. *J. Phys. Oceanogr.* **21**, 1740–1761.

Herbers, T. H. C. & Guza, R. T. 1992 Wind-wave nonlinearity observed at the sea floor. Part II. Wavenumbers and third order statistics. *J. Phys. Oceanogr.* **22**, 489–504.

HERBERS, T. H. C., LOWE, R. L. & GUZA, R. T. 1991 Field verification of acoustic Doppler surface gravity wave measurements. *J. Geophys. Res.* **96**, 17023–17035.

KOMEN, G. J. 1980 Nonlinear contributions to the frequency spectrum of wind-generated water waves. *J. Phys. Oceanogr.* **10**, 779–790.

KUIK, A. J., VLEDDER, G. PH. VAN & HOLTHUIJSEN, L. H. 1988 A method for the routine analysis of pitch-and-roll buoy data. *J. Phys. Oceanogr.* **18**, 1020–1034.

LAING, A. K. 1986 Nonlinear properties of random gravity waves in water of finite depth. *J. Phys. Oceanogr.* **16**, 2013–2030.

LHERMITTE, R. 1985 Water velocity and turbulence measurements by coherent Doppler sonar. In *Oceans 85*, pp. 1159–1164. IEEE.

LIU, P. L.-F., YOON, S. B. & KIRBY, J. T. 1985 Nonlinear refraction-diffraction of waves in shallow water. *J. Fluid Mech.* **153**, 185–201.

LONGUET-HIGGINS, M. S. 1963 The effect of non-linearities on statistical distributions in the theory of sea waves. *J. Fluid Mech.* **17**, 459–480.

LONGUET-HIGGINS, M. S., CARTWRIGHT, D. E. & SMITH, N. D. 1963 Observations of the directional spectrum of sea waves using the motions of a floating buoy. In *Ocean Wave Spectra*, pp. 111–136. Prentice-Hall.

LONGUET-HIGGINS, M. S. & STEWART, R. W. 1962 Radiation stress and mass transport in surface gravity waves with application to 'surf beats.' *J. Fluid Mech.* **13**, 481–504.

OKIHIRO, M., GUZA, R. T. & SEYMOUR, R. J. 1992 Bound infragravity waves. *J. Geophys. Res.* **97**, 11453–11469.

PEREGRINE, D. H. 1967 Long waves on a beach. *J. Fluid Mech.* **27**, 815–827.

PHILLIPS, O. M. 1960 On the dynamics of unsteady gravity waves of finite amplitude. Part 1. The elementary interactions. *J. Fluid Mech.* **9**, 193–217.

SIMPSON, J. H. 1969 Observations of the directional characteristics of sea waves. *Geophys. J. R. Astron. Soc.* **17**, 93–120.

THORNTON, E. B. & GUZA, R. T. 1983 Transformation of wave height distribution. *J. Geophys. Res.* **88**, 5925–5938.

THORNTON, E. B. & KRAPOHL, R. F. 1974 Water particle velocities measured under ocean waves. *J. Geophys. Res.* **79**, 847–852.

WEBB, S. C. & COX, C. S. 1986 Observations and modeling of seafloor microseisms. *J. Geophys. Res.* **91**, 7343–7358.